Talanta 176 (2018) 284–292

Contents lists available at ScienceDirect

Talanta

journal homepage: www.elsevier.com/locate/talanta

Nuclear forensics investigation of morphological signatures in the thermal decomposition of uranyl peroxide

Ian J. Schwerdt, Adam Olsen, Robert Lusk, Sean Heffernan, Michael Klosterman, Bryce Collins, Sean Martinson, Trenton Kirkham, Luther W. McDonald IV, *

University of Utah, Department of Civil and Environmental Engineering, Nuclear Engineering Program, 201 Presidents Circle, Salt Lake City, UT 84112, United States

ARTICLE INFO

Keywords:
Nuclear forensics
Quantitative morphology
Uranyl peroxide
Uranium trioxide
Microstructural fingerprint
Image Analysis

ABSTRACT

The analytical techniques typically utilized in a nuclear forensic investigation often provide limited information regarding the process history and production conditions of interdicted nuclear material. In this study, scanning electron microscopy (SEM) analysis of the surface morphology of amorphous-UO_3 samples calcined at 250, 300, 350, 400, and 450 °C from uranyl peroxide was performed to determine if the morphology was indicative of the synthesis route and thermal history for the samples. Thermogravimetic analysis-mass spectrometry (TGA-MS) and differential scanning calorimetry (DSC) were used to correlate transitions in the calcined material to morphological transformations. The high-resolution SEM images were processed using the Morphological Analysis for Material Attribution (MAMA) software. Morphological attributes, particle area and circularity, indicated significant trends as a result of calcination temperature. The quantitative morphological analysis was able to track the process of particle fragmentation and subsequent sintering as calcination temperature was increased. At the 90% confidence interval, with 1000 segmented particles, the use of Kolmogorov-Smirnov statistical comparisons allowed discernment between all calcination temperatures for the uranyl peroxide route.

1. Introduction

For interdicted nuclear materials, there is an increasing reliance on nuclear forensics for the identification of the nuclear material's source and route of diversion in order to mitigate the potential for additional illicit trafficking. Nuclear forensic analysis utilizes elemental, isotopic, chemical, and physical signatures to provide technical insight into the provenance (synthesis methods and procedures), and history of nuclear materials of an unknown origin [1]. These signatures can be the result of multiple factors including the starting materials, chemical synthesis and conversion conditions, neutron irradiation, physical processing (milling and grinding), and aging conditions. Understanding the impact of these parameters on the resulting product can improve the accuracy of nuclear attribution. Among the most important nuclear materials requiring well characterized forensic signatures is uranium and its associated oxide species.

The nuclear fuel cycle is initiated with the extraction of uranium-bearing ore from a mine. The uranium is recovered from the ore through leaching (acidic, basic, and/or in-situ), purified via solvent extraction or column chromatography, and precipitated through the addition of ammonia, magnesia, sodium hydroxide, ammonium hydroxide, or by the formation of $(UO_2)O_2(H_2O)_2{\cdot}2H_2O$ using hydrogen peroxide [2–4]. The precipitation of ammonium di-uranate (ADU) with gaseous ammonia or ammonium hydroxide was frequently used, but is now discouraged due to environmental concerns [5]. As a result of ammonia's environmental hazards, the increasing demand for higher purity uranium product, and the need to reduce contaminants from lower grade ores, there has been great interest in utilizing the hydrogen peroxide precipitation process. Several commercial plants have utilized the peroxide route since the 1960's, including the Rabbit Lake Uranium Mill in Canada [5], the Uranium Corporation of India Limited at Jaduguda Mines [6], and Atlas Minerals of Moab, UT [7].

The resulting precipitates may then be calcined to UO_3 or U_3O_8, or be directly reduced to UO_2. Commercially, the calcination of uranyl peroxide to UO_3 or U_3O_8 is often performed to increase product stability, improve product purity, and reduce shipping costs [8]. The calcination of uranyl peroxide to UO_3 occurs commercially at temperatures ranging from 260 to 450 °C, and for the calcination to U_3O_8 at temperatures of 700–800 °C [5,9–13]. To complicate matters further, depending upon the source material and the calcination temperature, the resulting UO_3 can consist of various crystalline polymorphs [14]. To this end, in this study, the morphology of a common polymorph

* Correspondence to: 110 Central Campus Drive, Suite 2000, Salt Lake City, UT 84112, United States.
E-mail address: luther.mcdonald@utah.edu (L.W. McDonald).

http://dx.doi.org/10.1016/j.talanta.2017.08.020
Received 30 June 2017; Received in revised form 4 August 2017; Accepted 5 August 2017
Available online 12 August 2017

from the uranyl peroxide route, amorphous-UO_3 (am-UO_3), was evaluated as a forensics identifier of the material's processing. In 1963, Cordfunke et al. synthesized am-UO_3 via the uranyl peroxide route from a uranyl nitrate solution [15]. They found that if the uranyl peroxide precipitate, $UO_4{\cdot}4H_2O$, was washed of any residual nitrates, and dried at 80 °C to form $UO_4{\cdot}2H_2O$, no apparent change in morphology occurred. Upon calcination at 425 °C, am-UO_3 was formed, and retained the morphology of the initial uranyl peroxide. Through additional heating to 500 °C, α-UO_3 would be formed. In contrast, if the residual nitrates were not washed from the uranyl peroxide precipitate, the drying process resulted in $UO_4{\cdot}2H_2O$ with a radically different morphology. Further calcination at 425 °C would produce α-UO_3, with no apparent change in morphology from the previously dried $UO_4{\cdot}2H_2O$. While the final product of both the washed and unwashed uranyl peroxide can be α-UO_3, Cordfunke et al. noted that the morphology of the resulting α-UO_3 can be drastically different [15]. From a nuclear forensic analysis viewpoint, this work indicates an analysis of surface morphology could narrow the source of a UO_3 material of unknown origin to a producer that does, or does not, wash their uranyl peroxide precipitates. In this study, the morphology of am-UO_3 from washing uranyl peroxide was quantified for the first time to assess the feasibility of this signature.

Historically, optical and electron microscopy have been used in the nuclear forensics community to gain qualitative insight about a sample, without compromising the sample's integrity. Examples of this form of qualitative morphological analysis can be seen in the work of Tamasi et al. [16–19], and Keegan et al. [20]. Ray et al. have advocated for the development of "microstructural fingerprints", which are a set of qualitative and quantitative signatures developed through microscopic analysis of powder nuclear materials that are indicative of thermal and process history [21]. There is a major need for quantitative parameters that can rapidly determine whether differences between an unknown sample and a reference standard are statistically significant. It would be even more beneficial if these parameters could elucidate not just the starting material speciation, but the processing conditions experienced by the sample.

Recently, Olsen et al. demonstrated the ability to perform quantitative morphological analysis of SEM images to identify the calcination history of α-U_3O_8 [22]. The following study builds upon this progress, demonstrating the quantitative morphological analysis of am-UO_3 as a function of calcination temperature. Differential scanning calorimetry (DSC), thermogravimetric analysis-mass spectrometry (TGA-MS), and powder X-ray diffractometry (p-XRD) were used to correlate morphological differences with chemical transitions.

2. Experimental methods

2.1. Materials and synthesis

The $UO_2(NO_3)_2{\cdot}6H_2O$ (International Bio-Analytical Industries, Inc., 99.9%) used in this study was first dissolved in 1% HNO_3 solution to make a 1.0 M uranyl nitrate solution. The synthesis of studtite, $(UO_2)O_2(H_2O)_2{\cdot}2H_2O$, from $UO_2(NO_3)_2{\cdot}6H_2O$ and 30% H_2O_2 (EMD Millipore, Suprapur™ grade) was described in detail previously [22]. The filtered and washed studtite was allowed to dry at room temperature overnight. Subsequently, metastudtite, $(UO_2)O_2(H_2O)_2$, was prepared by dehydrating the studtite for 24 h at 80 °C. The metastudtite was ground in a high-purity aluminum oxide mortar and pestle. Powder X-ray diffractometry (p-XRD) confirmed the purity of the resulting metastudtite. Approximately 100 mg of metastudtite was placed in 5 mL platinum crucibles for calcination in an atmosphere-controlled furnace. Amorphous-UO_x ($3 \le x \le 3.5$) was synthesized from the metastudtite material at calcination temperatures of 250, 300, 350, 400, and 450 °C in triplicate under a flow of 500 mL/min of purified air. The furnace was ramped to temperature at a rate of 2.5 °C/min., held at the target calcination temperature for 8.25 h., then ramped down at a rate of 0.625 °C/min. While not undergoing processing or analysis, the samples were stored at room temperature in a vacuum chamber at 20kPa.

2.2. Powder X-ray diffraction (p-XRD) analysis

Powder XRD patterns of the starting material and various calcination products were collected at room temperature on a Philips Panalytical X'Pert diffractometer using Cu Kα X-rays (λ=1.5418 Å) operating at 40 kV and 40 mA. Continuous scans were performed over the range of 15–90° 2Θ with a step size of 0.020° and a scan speed of 0.04°/second. All samples consisted of 70–90 mg of U-oxide, and they were characterized on quartz slides with a limited background.

2.3. Differential Scanning Calorimetry (DSC)

Differential scanning calorimetry (DSC) was performed using a Netzsch DSC 3500 Sirius. A baseline was acquired using an empty aluminum pan within 12 h of running the metastudtite samples. Metastudtite samples of ca. 20 mg were placed in aluminum pans with pierced lids, and heated at a rate of 10 °C/min from 20 °C to 600 °C. At a rate of 40 mL/min, dry nitrogen was flowed over the aluminum pans. The large sample size allows for an increased sensitivity to transitions, but at the expense of decreased resolution, due to increased thermal lag. Empty aluminum pans with pierced lids were utilized as a reference signal for each run.

2.4. Thermogravimetic Analysis-Mass Spectrometry (TGA-MS)

Thermogravimetic analysis combined with online mass spectrometry (TGA-MS) was performed using a TA Instruments SDT Q600 coupled with a Pfeiffer ThermoStar GSD 320 T3 that contains a PrismaPlus mass spectrometer. Metastudtite samples of ca. 60 mg were placed in alumina crucibles, and purged in the TGA furnace with helium (100 mL/min) for 60 min at room temperature to reduce any atmospheric air signatures in the mass spectrometer. The samples were then heated at a rate of 10 °C/min from 25 °C to 600 °C, and held at 600 °C for 1 h, in a flowing atmosphere of 100 mL/min high-purity helium. The decomposition product gases were fed through a heated capillary column (150 °C) into the mass spectrometer. The mass spectrometer was operated in a selected ion mode targeting the following ions: m/z=14 (N^+), 16 (O^+), 17 (OH^+), 18 (H_2O^+), 30 (NO^+), 32 (O_2^+), and 46 (NO_2^+).

2.5. Scanning Electron Microscopy (SEM)

The initial metastudtite and the 15 am-UO_x samples were prepared for SEM by dusting 5–10 mg of each sample on top of a 12 mm conductive carbon tab that was adhered to a 12.7 mm aluminum pin stub mount. Loosely held sample was removed by firmly tapping the side of the SEM stub mounts. Using a Gatan 682 Precision Etching and Coating System (PECS) the samples were sputter coated with 20.2 ± 0.1 nm of Au/Pd film to reduce charging. Images of the samples were collected with a FEI Quanta 600 FEG scanning electron microscope at an accelerating voltage of 12 kV. Images were acquired using both the Everhart-Thornley secondary electron (SE) and solid-state diode back scattered electron (BSE) detectors. The BSE detector provided Z-contrast for the sample images. The SE detector was more sensitive to surface-generated secondary electrons and provided images of the surface topography with high resolution. Within each sample, 3–4 macro-particles were selected for thorough examination. For each macro-particle, at least 10 images were acquired across a wide area of the macro-particle surface at magnifications of 15,000–30,000x. Over the entire range of calcination temperatures, more than a thousand SEM images were acquired, providing a large population of images for statistical analysis.

2.6. Quantitative morphology analysis

The quantitative measurement of the imaged morphological features was performed using the Morphological Analysis for Materials (MAMA) Version 2.1 software developed at Los Alamos National Laboratory [23]. The 2–3 highest resolution SEM images for each macro-particle acquired with the SE detector were selected for particle segmentation analysis. The detailed procedure for particle segmentation was presented previously [22]. The use of manual particle segmentation allows for the undesired effect of individual user bias. To replicate and account for the variance likely to be encountered by real-world user bias, the SEM images from each calcination temperature were evenly divided among four investigators. A number of surface feature attributes; such as, circularity, pixel area, ellipse aspect ratio, and equivalent circular diameter (ECD) were quantified for at least 1000 surface features from each evaluated temperature. The resulting data was statistically analyzed using a Kolmogorov-Smirnov (K-S) two-sample test implemented in MATLAB R2015b [24]. Additional data analysis was performed using JMP Pro Version 13.1.0 [25].

3. Results and discussion

3.1. Thermal decomposition analysis

While quantifying the morphological features of U-oxides will greatly improve our ability to use these signatures for nuclear forensics, understanding the chemical processes that impact the morphology is equally important to expand our fundamental understanding of the limitations of this signature. Hence, to understand the implications of any identified morphological changes as a function of calcination temperature, DSC, p-XRD, and TGA/MS were used to monitor the thermal decomposition of metastudtite. The p-XRD results confirmed the starting material was pure metastudtite, $(UO_2)O_2(H_2O)_2$ (Fig. 1).

In correlating the DSC and TGA data, a subtle endothermic peak at 102 °C is observed in the DSC thermogram (Fig. 3), which correlates with a mass loss of 1.23 ± 0.30% (3σ error reported) on the TGA (Fig. 3). This endothermic peak is attributed to the loss of adsorbed atmospheric water, or a small amount of residual studtite that was below the approximately 5% detection limit typical for p-XRD [26]. Starting at 210 °C, the DSC curve gives a significant endothermic peak, and the TGA reveals a significant mass loss, 13.34 ± 0.07%, from 150 to 250 °C. The theoretical weight loss for the conversion of $(UO_2)O_2(H_2O)_2$ to am-U_2O_7 (corresponding to $(UO_2)OO_{0.5}$ [27]), or am-UO_3 is 12.95% and 15.31%, respectively. A significant increase in H_2O and O_2 was detected on the mass spectrometer during this mass loss. No additional H_2O peaks were seen throughout the remainder of the heating process, indicating that the am-UO_x ($3 \le x \le 3.5$) produced is anhydrous. While p-XRD confirmed that the calcination of the starting material at 250 °C produced amorphous material (Fig. 2), am-U_2O_7 or am-UO_3 could not be distinguished. Nonetheless, based on the experimental mass loss, and the concomitant release of O_2 and H_2O, the product most likely formed is am-U_2O_7. This result is consistent with the TGA/MS and IR results of Guo et al. [27], Sato [28], and Odoh et al. [29].

As the temperature is increased, the TGA shows a continual loss in

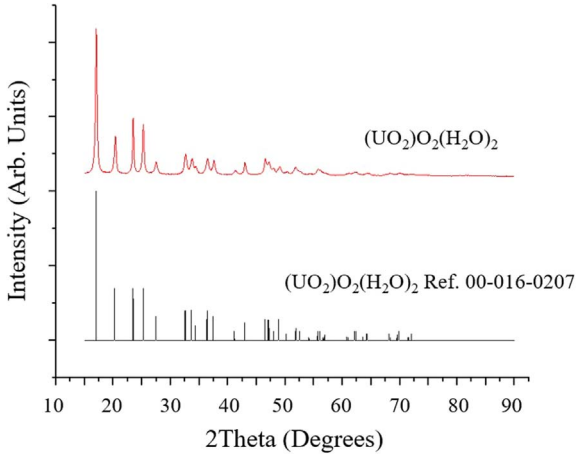

Fig. 1. Powder X-ray diffraction patterns for the starting $(UO_2)O_2(H_2O)_2$ compared to the metastudtite Reference 00–016.

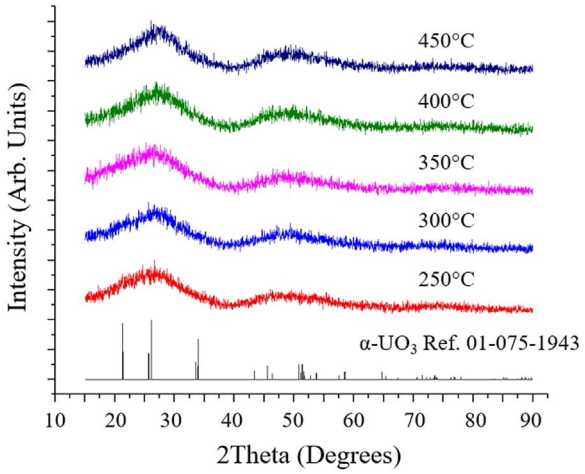

Fig. 2. Powder X-ray diffraction patterns for the calcination products from the thermal decomposition of uranyl peroxide held at the listed temperatures for 8.25 h in air. The samples calcined at 250–450 C were confirmed to be X-ray amorphous.

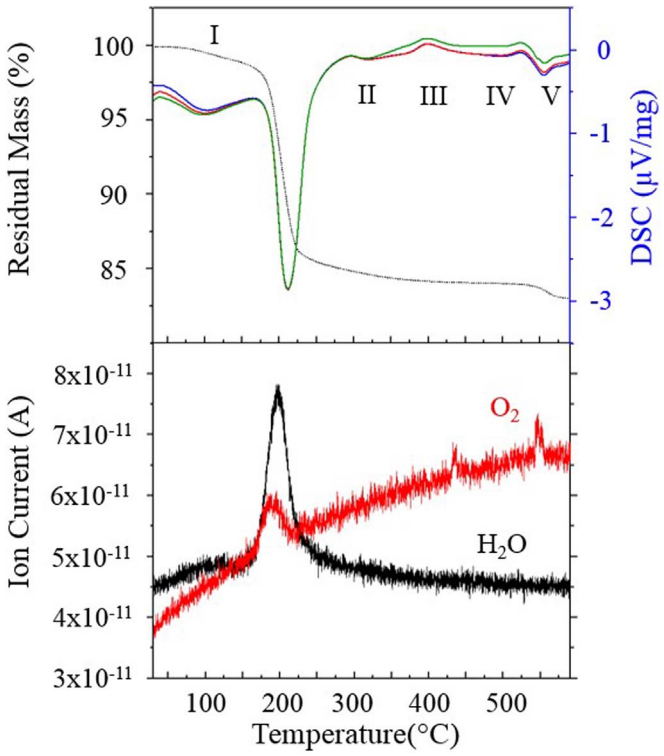

Fig. 3. Top) TGA results and DSC thermogram, with exothermic transitions occurring in the upward direction, three DSC replicates displayed. I= $(UO_2)O_2(H_2O)_2$, II= am-U_2O_7, III=am-UO_3, IV=α-$UO_{2.9}$, V= α-U_3O_8, Bottom) Mass spectrometer readings for O_2 and H_2O as metastudtite was heated from 25 °C to 600 °C at 10 °C/min. The first increase in O_2 and H_2O at 200 °C coincides with the dehydration and decomposition of $(UO_2)O_2(H_2O)_2$ to am-U_2O_7. The second O_2 increase at 425 °C likely is the result of the conversion of am-U_2O_7 to am-UO_3. The third O_2 increase at 550 °C is attributed to the conversion of am-UO_3 to α-$UO_{2.9}$/α-U_3O_8.

mass that temporarily plateaus between 400–500 °C. A significant mass loss of 14.76 ± 0.09% by 450 °C is observed. This is relatively close to the expected mass loss of 15.31% for the conversion of $(UO_2)O_2(H_2O)_2$ to am-UO_3. P-XRD of the 300, 350, 400, and 450 °C calcination products confirm the material to be x-ray amorphous (2). A subtle exothermic peak is registered at 400 °C by the DSC, and an increase in O_2 was observed in the mass spectrometer at 425 °C (Fig. 2). This mass spectrometer signal is consistent with a similar increase observed by Guo et al. [27] at 500 °C, while investigating the decomposition of studtite in argon. In that study, a small change in mass, also appears to occur, but without the accompanying exothermic transition. The O_2 signal with associated mass loss was attributed to the transition of am-U_2O_7 to am-UO_3. In the current study, no significant abrupt change in mass appears to occur at this transition from am-U_2O_7 to am-UO_3. The discrepancy in onset temperatures between these results and those of Guo et al. [27] is most likely explained by the difference in starting materials. For example, Sato [28] previously demonstrated that the thermal transformation of metastudtite to α-UO_3 will occur at lower temperatures than the same transformation when starting with studtite [28]. The next exothermic transition occurs at 525 °C and is associated with the transition of am-UO_3 to α-$UO_{2.9}$. The exothermic peak is rapidly followed by an endothermic transition at 555 °C. The theoretical mass loss for the conversion of metastudtite to α-$UO_{2.9}$ and α-U_3O_8 is 15.79% and 16.89% respectively. The experimental mass loss by 570 °C was 15.66 ± 0.09%, closely matching the expected value for α-$UO_{2.9}$. The sample was held at a temperature of 600 °C for 1 h, undergoing a continuous change in mass, achieving a total mass loss of 16.11 ± 0.09%. P-XRD scans of samples calcined for 8 h at 570 °C and 600 °C both indicate a mixture of α-UO_3 and α-U_3O_8 (Figure A.1). The unexpected presence of α-UO_3 instead of α-$UO_{2.9}$ in the ex-situ room temperature p-XRD scans has been encountered previously, and was proposed to be due to either α-$UO_{2.9}$ instability at room temperature in atmospheric air, or the slow kinetics of conversion of α-UO_3 to α-$UO_{2.9}$ [15,28,30]. Based on the 8-h calcination run at 570 °C resulting in no detectable traces of α-$UO_{2.9}$ in ex-situ p-XRD, the cause is likely α-$UO_{2.9}$ instability in air.

3.2. Surface morphology analysis

Given that the calcination products formed from the thermal decomposition of metatstudtite in the range of 250–450 °C were all confirmed to be x-ray amorphous, p-XRD analysis provides limited insight into the material process history. In an effort to identify forensics signatures indicative of calcination temperature, both qualitative and quantitative SEM image analyses of surface features were performed. Representative SEM images acquired for these samples can be seen in Fig. 4. The lexicon of descriptors for nuclear material images developed by Tamasi et al. can be applied to the am-UO_x calcination product images for qualitative analysis purposes [17,19].

Qualitatively, the macro-particles present in the images of the starting material and the 250–450 °C calcination products all consisted of similar *clumped/massive agglomerates* that exhibited a wide range of particle diameters (10–500 μm). The macro-particles were *sub-rounded*, of *medium* to *high sphericity,* and had a *somewhat rough* surface. The micro-particles present ubiquitously across the larger grains, at all temperatures, were of a *rounded/blocky* overall morphology, with a distribution of particle edges ranging from *sub-rounded* to *sub-angular*. The micro-particles consisted of a mixture of *irregular clumps composed of anhedral prolate* grains in the majority, or *subhedral columnar* grains in the minority. The *prolate* and *columnar* micro-particles visible in the metastudtite starting material do not appear to be significantly transforming in general shape as a function of calcination temperature. As the calcination temperature increased, the larger *prolate* micro-particles had a tendency to crack/fracture into approximately 2–4 smaller fragments that in composite were indicative of the *prolate* structure. The fracturing has been hypothesized to be due to oxygen escape and thermal strain [15]. At a calcination temperature of 450 °C, there was evidence that some of the cracks/fractures were sintering, resulting in particle bridge growth. Plaue previously noted the onset of particle sintering at temperatures as low as 400 °C in his SEM analysis of the calcination products from washed uranyl peroxide [31].

Void spaces were a prevalent feature throughout all the samples, occurring to some extent in almost all the images acquired in the 15,000–25,000x magnification range. The voids frequently occurred between the larger *irregular clumps of sub-rounded grains*, and appeared to generally be the result of larger cracks running across the macro-particle surface. It was anticipated that the void space area coverage would increase at higher calcination temperatures as a result of dehydration cracking and increased thermal strain. Upon microscopic inspection, the void space area coverage qualitatively appeared to decrease with increasing calcination temperature, with the 450 °C calcination product material exhibiting the least amount of void space coverage. The previously mentioned high-temperature micro-particle fracturing could result in smaller particulate that better “fills” the void spaces as well as sintering processes causing increased densification of the macro-particles.

Tamasi et al. previously investigated the qualitative morphology of α-UO_3 calcined at 485 °C from metastudtite synthesized through peroxide precipitation in uranyl chloride solution [19]. In that study, the precipitation pH was adjusted to 3.0 through the addition of ammonium hydroxide. In the current work, no additional reagents were utilized to control the pH, and a pH of 1 was present during the precipitation. Kim et al. has previously noted that the uranyl peroxide particle size tends to decrease with increasing solution pH [32]. The macro- and micro-particles in that study displayed very similar morphologies to this current work, and many of the qualitative descriptors are aligned. One notable difference is the presence of the subhedral columnar grains in the current work, which are likely a result of differences in the precipitation conditions. The peroxide precipitation route in a uranyl nitrate system is known to result in particles exhibiting a more columnar or acicular character, with the resulting morphology being highly reliant on the uranium and nitrate concentration [15,30,32,33].

The qualitative SEM analysis results corroborate what has been identified previously, that the thermal decomposition of washed metastudtite occurs pseudomorphically. The $(UO_2)O_2(H_2O)_2$ starting material and the am-UO_x calcination products exhibiting morphologies that are markedly similar, while being distinct chemical species [15,19,30]. The morphological signature of the starting material, being carried through into the calcination products, allow one to trace back to the likely synthetic route for the initial uranium ore concentrate. The qualitative analysis in this study did not identify any readily identifiable difference in the resulting am-UO_x products as a function of the calcination temperature, limiting the forensics value of the SEM images. With the advent of new imagery analysis software, quantitative analysis was pursued to elucidate any significant differences in am-UO_x surface morphology that could act as a unique signature of the calcination temperature. In order to perform this quantitative analysis, the surface features must first be identified and segmented. To that end, the Morphological Analysis for Material Attribution (MAMA) Version 2.1 software developed at Los Alamos National Laboratory was utilized based on methods and criteria described previously [22].

The XRD and quantitative morphological results of metastudtite thermal decomposition to α-U_3O_8 in the range of 600–800 °C were presented in a previous study [22]. The morphological data was modified in presentation and included in this study to allow for a comparison of the quantitative morphology of both am-UO_x and α-U_3O_8 resulting from the calcination of similar uranyl peroxide precursors at temperatures ranging from 250 to 800 °C. No attempt was made to quantify the macro-particle features. The macro-particles are likely susceptible to modification through grinding and other physical

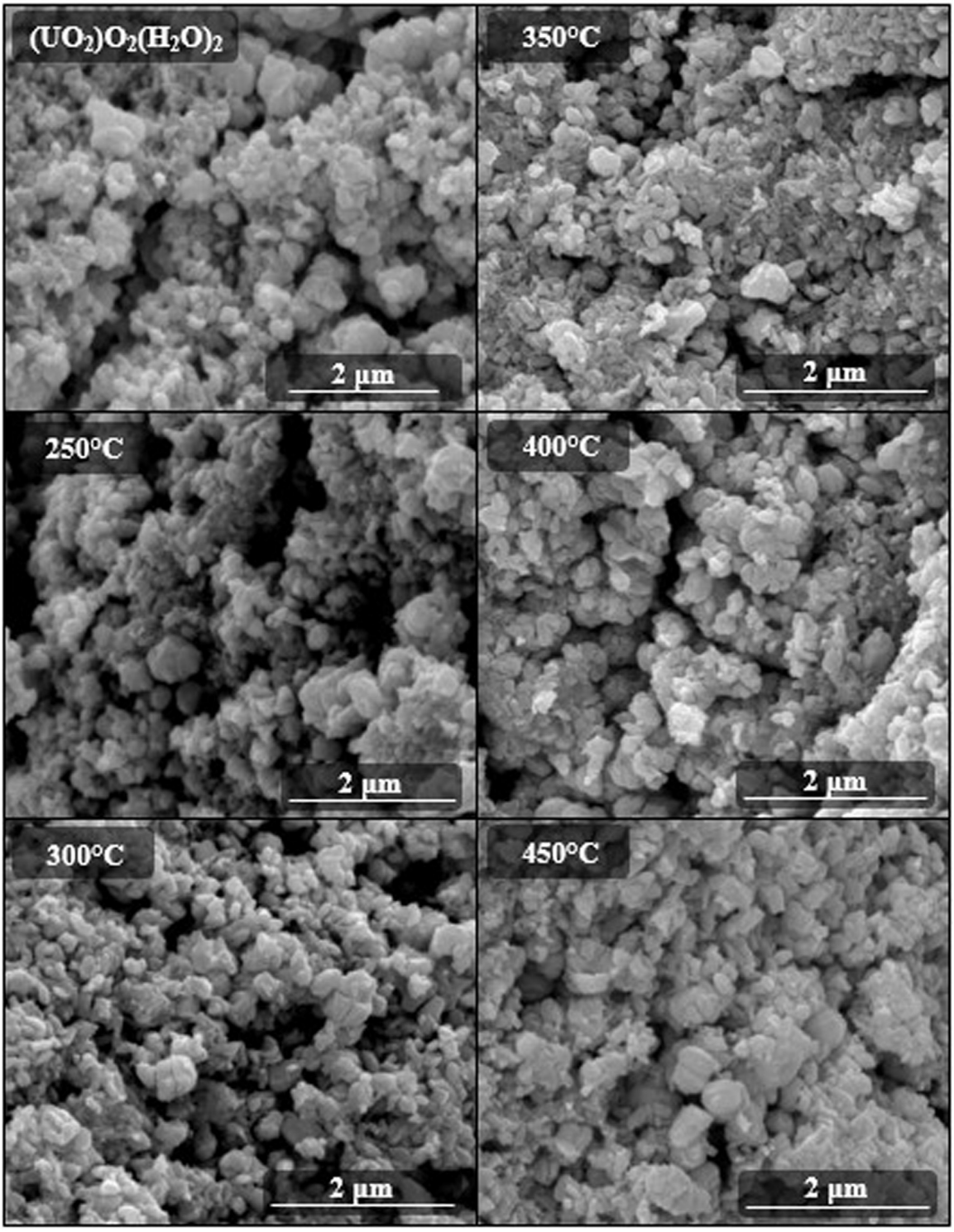

Fig. 4. Representative SEM Images of the metastudtite starting material and the resulting calcination products generated at temperatures of 250 °C, 300 °C, 350 °C, 400 °C, and 450 °C.

processing. It has previously been noted that the quantitative analysis of macro-particle parameters is also susceptible to bias, or is a poor indicator of calcination temperature history [34–36]. The micro-particles with well-defined boundaries present on the surface of the calcination products were the target feature of the quantitative analysis.

The manual segmentation results for one of the analyzed images can be seen in Fig. 5. It is worth noting that only a small portion of the surface features meet the inclusion criteria, as outlined previously [22]. A minimum of 1000 particles were quantified for each calcination temperature skew. A number of quantified morphological attributes demonstrated significant variation as a function of temperature (see supplemental Figure A.2–A.12), but pixel area and circularity showed the greatest promise for process history discernment. The quantitative result for the pixel area attribute, which is the area based on multiplying the number of pixels contained within the object boundary by a pixel to physical scale conversion, is reported in Fig. 6 [37]. The circularity attribute, which is calculated using the isoperimetric quotient where a circularity value of unity corresponds to a perfect circle, is reported in Fig. 7 [37].

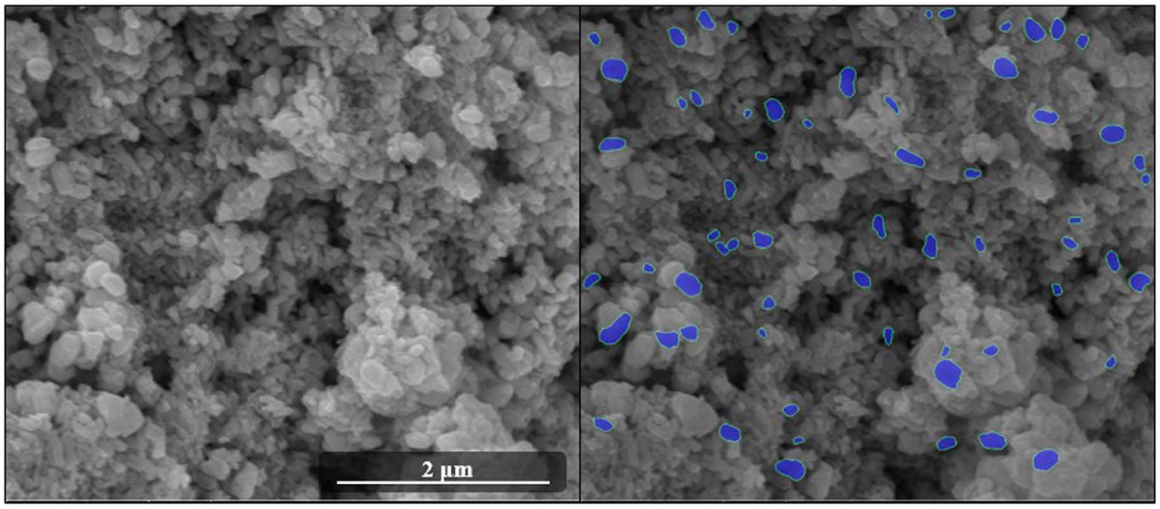

Fig. 5. SEM images of am-UO_3 formed at a calcination temperature of 450 °C. SEM image prior to MAMA segmentation (left). SEM image following segmentation in MAMA (right). The blue marks are surface features that were manually segmented utilizing an inclusion criterion that was presented previously [39]. Some notable characteristics of the inclusion criteria include particles that are unobstructed, have well defined boundaries, and are of sufficient size (> 15 pixels). Same scale for both images.

The pixel area results show that the particle size decreases as the calcination temperature increases from 250 °C to 400 °C, achieves a minimum in the range of 400–600 °C, and increases in size from 600 °C to 800 °C. The quantitative analysis results corroborate what was described in the qualitative analysis. The surface grains appear to undergo fracturing and grain splitting until a calcination temperature of 400 °C, resulting in smaller segmented surface features. At a temperature of 400–450 °C, the surface grains begin to sinter, and larger segmented features result. The α-U_3O_8 samples exhibited a continuous increase in pixel area with increasing temperature, which was attributed to the sintering process [22].

Thomas et al., while investigating the calcination of washed uranyl peroxide, found that the specific surface area (SSA) increased from 250 °C to 400 °C, and then noted a sharp decrease from 400 to 450 °C, and the surface area continued to decrease as the calcination temperature was increased [30]. Plaue also identified a significant decrease in SSA as the uranyl peroxide calcination temperature was increased from 400 °C to 600 °C [31]. Hastings et al. found that for the calcination of uranyl peroxide, the resulting UO_3 exhibited an 8% decrease in material density from 350 °C to 450 °C, which was ascribed to sintering [38]. These studies correlate well with the results of the quantitative pixel area data and the qualitative analysis of the SEM images. Supporting the view that as the particles are dehydrating and undergoing thermal strain that causes particle fracturing in the low temperature region, the result is increased surface area and smaller particle size. As sintering and bridge growth starts to occur at higher temperatures, the particle size increases, and the surface area decreases. The transition from am-U_2O_7 to am-UO_3 registered on the DSC and TGA-MS occurs in the region of 400 °C, and could also be a possible explanation for the inflection in particle area at this temperature.

The circularity results in Fig. 7 indicate a continual increase in circularity as the calcination temperature is increased. It was anticipated that the greatest increase in circularity would coincide with the onset of particle sintering and grain suturing in the realm of 350 °C to 450 °C, as was seen in the qualitative analysis. In actuality, the greatest increase in circularity occurred at the lower temperatures of 250 °C to 300 °C. These low temperature changes in circularity were not identified in the qualitative analysis, and only were illuminated through the use of quantitative morphological analysis. The circularity increases consistently from 450 °C to 800 °C as the am-UO_3 is converted to α-U_3O_8 as a result of grain suturing and sintering. It was qualitatively noted by Olsen et al., that as the calcination temperature increased from 600 °C to 800 °C the prevalence of *sub-rounded/rounded* grains correspondingly increased as a result of sintering [39].

The 99% confidence intervals on the mean of each temperature for both the pixel area and circularity attributes suggest that the calcination temperature results in statistically significant morphological differences, but further statistically rigorous analysis was performed to determine the minimum number of micro-particles required for statistical significance between the calcination temperatures. Manual segmentation of microparticle features can be time and labor intensive; therefore, minimizing the number of particles that need to be segmented for statistical relevance, would improve the nuclear forensic analysis timeline. Vigneau et al. previously developed a method for

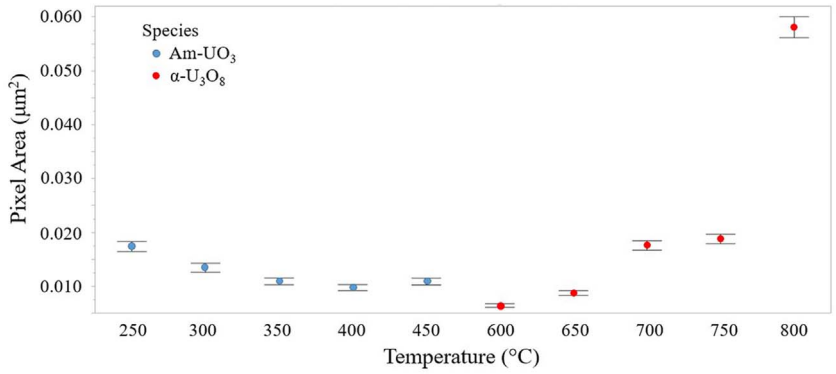

Fig. 6. Pixel area of UO_3 and U_3O_8 as a function of calcination temperature from manually segmented SEM images. The error bars correspond to the 99% confidence interval for the mean of each group. Pixel area exhibits a minimum in the temperature range of 400–600 °C. U_3O_8 data modified from Olsen et al. [22].

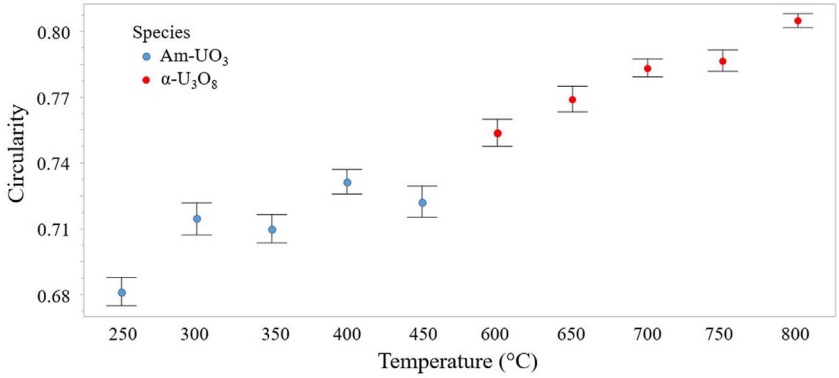

Fig. 7. Circularity of UO_3 and U_3O_8 as a function of calcination temperature from manually segmented SEM images. The error bars correspond to the 99% confidence interval for the mean of each group. Increase in circularity clearly exhibited for increasing calcination temperatures. U_3O_8 data modified from Olsen et al., [22].

determining the minimal number of particles that must be analyzed in an image(s) to have a reliable estimation of a particle size distribution [40]. This method was further developed and utilized for nuclear forensic purposes by Olsen et al. [22]. Following those methods, a two-sample Kolmogorov-Smirnov (K-S) test was utilized to perform pairwise comparisons between a sampled microparticle attribute distribution against a reference population of segmented microparticles for the 250, 300, 350, 400, and 450 °C calcination temperatures.

The K-S test compares the cumulative distribution functions between two micro-particle sample sets, and dependent on the desired confidence level, determines whether the two distributions are statistically distinct. The K-S test utilizes a scalar test statistic that is a measure of the maximum absolute vertical distance between the two sample distribution functions, denoted as D_{max}. The K-S test statistic is evaluated against a calculated threshold statistic, $D_{critical}$, which is a function of the respective sample sizes of the two distribution functions and the desired confidence level. If D_{max} is greater than $D_{critical}$, then the two distributions are statistically distinct at the evaluated confidence level [22,41].

To perform this evaluation on the quantified morphological data, MATLAB's data sample function was used to randomly sample distributions consisting of 500, 750, and 1000 segmented micro-particles from each temperature, and compared them pairwise against the full population of one temperature using the K-S test. The $D_{critical}$ value was evaluated at a desired confidence level of 90% and 99% for each distribution comparison. In Fig. 8, the results of the comparison of the full population of micro-particle area for 350 °C against random samples of 500, 750, and 1000 micro-particles from the 250 °C, 300 °C, 400 °C, and 450 °C populations are presented. The results indicate that utilizing quantified particle area, the 250 °C and 300 °C can be statistically discerned at the 99% confidence level with as little as 500 segmented particles. The 400 °C sample cannot be assessed as significantly different from the 350 °C population at a 99% confidence level until at least 1000 micro-particles have been segmented. The 450 °C sample cannot be assessed as significantly different from the 350 °C population at even the 90% confidence level, regardless of the number of micro-particles segmented. Repeating the analysis for the other calcination temperatures, similar results were seen. At the 90% confidence level, with the exception of 350 °C and 450 °C, 500 particles are sufficient for statistical discernment of all other temperatures. At the 99% confidence level, again with the exception of 350 °C and 450 °C, 1000 segmented particles are necessary for the discernment of calcination temperature using the particle area. The results of the comparisons for all the other calcination temperature populations can be seen in Supplemental Figs. A.13, A.15, A.17, A.19.

This evaluation was repeated for the micro-particle circularity distributions by temperature. The circularity attribute was much less effective at discerning calcination temperature, especially for the 300–350 °C and 400–450 °C comparisons. The diminished effectiveness of the circularity attribute relative to the particle area was demonstrated previously for α-U_3O_8 synthesized in the range of 600–800 °C [22]. This difficulty is evidenced in Fig. 9, which shows the results of the comparison of the full population of micro-particle circularity for 350 °C against random samples of 500, 750, and 1000 micro-particles from the 250 °C, 300 °C, 400 °C, and 450 °C populations. The 300 °C and 350 °C distributions cannot be discerned at the 90% confidence level, regardless of the number of segmented particles. Interestingly, the 450 °C distribution is statistically different from the 350 °C population at the 90% confidence level if 1000 particles are incorporated into the analysis. This suggests that while particle area alone may

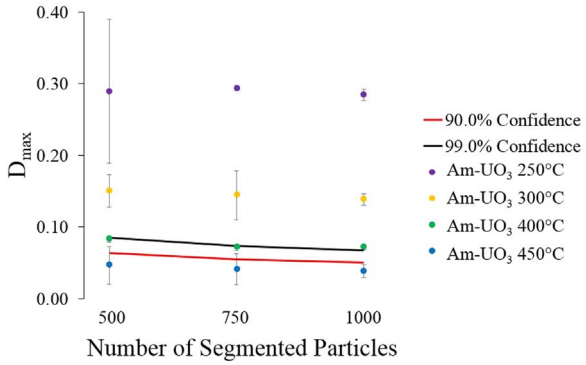

Fig. 8. Comparison of the particle area distributions to the full population distribution of segmented particles at 350 °C. At a sample size of 1000 particles, all the distributions were statistically different from the 350 °C population, with the exception of 450 °C, at the 99% confidence interval. All reported error is the 3σ of the calculated D_{max} value for each of the random sample sets.

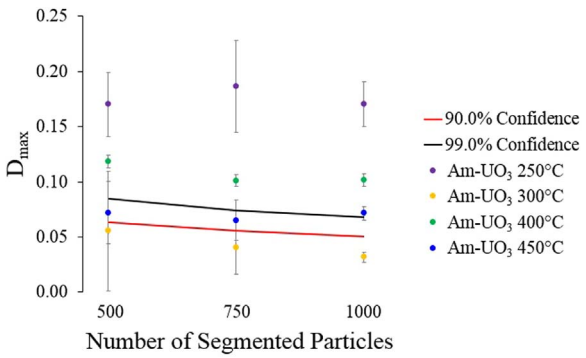

Fig. 9. Comparison of the particle circularity distributions to the full population distribution of segmented particles at 350 °C. At a sample size of 1000 particles, all the distributions were statistically different from the 350 °C population, with the exception of 300 °C, at the 99% confidence interval. All reported error is the 3σ of the calculated D_{max} value for each of the random sample sets.

not allow the differentiation of 350 °C and 450 °C, when coupled with the circularity attribute, these temperatures can be discerned at the 90% confidence level with 1000 segmented particles. When the particle area and circularity distributions are both evaluated, all the calcination temperatures are statistically different at the 90% confidence level with 1000 particles. The results of the circularity comparisons for all the other calcination temperature populations can be seen in Figs. A.14, A.16, A.18, A.20.

4. Conclusion

Qualitative morphological parameters traditionally provide Supplementary information in nuclear forensic investigations, but tell a limited portion of an unknown sample's story. The development of quantitative signatures that can provide statistically rigorous information regarding not just the chemical speciation, but the processing conditions of synthesis, would be a valuable addition to the forensic investigator's toolkit. In this work, it was shown that the decomposition of uranyl peroxide at temperatures of 250, 300, 350, 400, and 450 °C results in am-UO_x ($3 \leq x \leq 3.5$) with no readily identifiable difference in the p-XRD patterns. Through the application of quantitative morphological analysis on acquired SEM images, significant changes in particle area and circularity were observed. The presented application of the K-S test allowed statistical evaluation of the quantitative data, and allowed for discernment of calcination temperature at the 90% confidence level for 1000 segmented particles. This work demonstrates that in the absence of quantifiable p-XRD results, quantitative morphological analysis can provide insights into the calcination temperature history of am-UO_x from uranyl peroxide decomposition.

Acknowledgements

This synthesis of am-UO_3 and their subsequent characterization by p-XRD, SEM, TGA-MS, and DSC was supported by the U.S. Department of Homeland Security, Domestic Nuclear Detection Office, under Grant Award Number 2015-DN-077-ARI092. The same DHS grant, along with the Defense Threat Reduction Agency, under Grant Award Number HDTRA1-16-1–0026 supported the quantitative analysis via MAMA. The views and conclusions contained in this document are those of the authors and should not be interpreted as necessarily representing the official policies, either expressed or implied, of the U.S. Department of Homeland Security or Defense Threat Reduction Agency. This work made use of University of Utah Shared facilities of the Surface Analysis and Nanoscale Imaging Group sponsored by the College of Engineering, Health Sciences Center, Office of the Vice President for Research, and the Utah Science Technology and Research (USTAR) Initiative of the State of Utah. This work made use of the Materials Characterization Lab at the University of Utah. The authors would like to thank Dana W. Overacker for providing access to the TGA-MS equipment.

Appendix A. Supporting information

Supplementary data associated with this article can be found in the online version at doi:10.1016/j.talanta.2017.08.020.

References

[1] K.J. Moody, P.M. Grant, I.D. Hutcheon, Nuclear Forensic Analysis, 2nd ed., CRC Press, 2015.
[2] C.R. Edwards, A.J. Oliver, Uranium processing: a review of current methods and technology, JOM 52 (9) (2000) 12–20.
[3] M.I. Pownceby, C. Johnson, Geometallurgy of Australian uranium deposits, Ore Geol. Rev. 56 (2014) 25–44.
[4] P.D. Wilson, The Nuclear Fuel Cycle: From Ore to Wastes, Oxford University Press, 1996.
[5] I.A.E. Agency, Uranium Extraction Technology, IAEA Technical Report Series, 1993.
[6] R. Gupta, V.M. Pandey, S.R. Pranesh, A.B. Chakravarty, Study of an improved technique for precipitation of uranium from eluted solution, Hydrometallurgy 71 (3–4) (2004) 429–434.
[7] F. Caropreso, W. Badger, Hydrogen peroxide precipitation of uranium at the Atlas minerals uranium mill, Trans. Soc. Min. Eng. AIME 254 (1973).
[8] G. Jobling, Apparatus for the production of yellowcake from a uranium peroxide precipitate, Google Patents, 2011.
[9] A. Hammad, H. Serag, A. Abdallah, Preparation of Nuclear Pure Uranium Trioxide from El-Atshan Crude Yellow Cake Using Tri Octyl Phosphine Oxide, in: Proceedings of the Second Arab Conference on the Peaceful Uses of Atomic Energy, p. 245.
[10] J. Litz, R. Coleman, A Review of United States Yellow Cake Precipitation Practice, IAEA, Paris, 1979, pp. 101–117.
[11] C.D. Harrington, A.E. Ruehle, Uranium Production Technology, Van Nostrand, 1959.
[12] A.A. Adam, M.A.H. Eltayeb, O.B. Ibrahim, Uranium recovery from Uro area phosphate ore, Nuba Mountains, Sudan, Arab. J. Chem. 7 (5) (2014) 758–769.
[13] A. Bonini, J. Cabrejas, L. de Lio, L. Dell'Occhio, C. Devida, G. Dupetit, M. Falcon, A. Gauna, D. Gil, G. Guzman, P. Neuringer, A. Pascale, A. Stankevicius, Nuclear fuel cycle head-end enriched uranium purification and conversion into metal, In: Proceedings of the International meeting on reduced enrichment for research and test reactor (RERTR), Sao Paulo, Brazil, 1998, pp. 1-10.
[14] H.R. Hoekstra, S. Siegel, The uranium-oxygen system: U3O8□UO3, J. Inorg. Nucl. Chem. 18 (1961) 154–165.
[15] E.H.P. Cordfunke, A.A. Van Der Giessen, Pseudomorphic decomposition of uranium peroxide into UO3, J. Inorg. Nucl. Chem. 25 (5) (1963) 553–555.
[16] A.L. Tamasi, K.S. Boland, K. Czerwinski, J.K. Ellis, S.A. Kozimor, R.L. Martin, A.L. Pugmire, D. Reilly, B.L. Scott, A.D. Sutton, G.L. Wagner, J.R. Walensky, M.P. Wilkerson, Oxidation and hydration of U3O8 materials following controlled exposure to temperature and humidity, Anal. Chem. 87 (8) (2015) 4210–4217.
[17] A.L. Tamasi, L.J. Cash, C. Eley, R.B. Porter, D.L. Pugmire, A.R. Ross, C.E. Ruggiero, L. Tandon, G.L. Wagner, J.R. Walensky, A.D. Wall, M.P. Wilkerson, A lexicon for consistent description of material images for nuclear forensics, J. Radioanal. Nucl. Chem. 307 (3) (2016) 1611–1619.
[18] A.L. Tamasi, L.J. Cash, W.T. Mullen, A.L. Pugmire, A.R. Ross, C.E. Ruggiero, B.L. Scott, G.L. Wagner, J.R. Walensky, M.P. Wilkerson, Morphology of U3O8 materials following storage under controlled conditions of temperature and relative humidity, J. Radioanal. Nucl. Chem. 311 (1) (2017) 35–42.
[19] A.L. Tamasi, L.J. Cash, W. Tyler Mullen, A.R. Ross, C.E. Ruggiero, B.L. Scott, G.L. Wagner, J.R. Walensky, S.A. Zerkle, M.P. Wilkerson, Comparison of morphologies of a uranyl peroxide precursor and calcination products, J. Radioanal. Nucl. Chem. (2016).
[20] E. Keegan, M.J. Kristo, M. Colella, M. Robel, R. Williams, R. Lindvall, G. Eppich, S. Roberts, L. Borg, A. Gaffney, J. Plaue, H. Wong, J. Davis, E. Loi, M. Reinhard, I. Hutcheon, Nuclear forensic analysis of an unknown uranium ore concentrate sample seized in a criminal investigation in Australia, Forensic Sci. Int. 240 (2014) 111–121.
[21] I. Ray, A. Schubert, M. Wallenius, The concept of a microstructural fingerprint for characterization of samples in nuclear forensic science, in: Proceedings of the International Conference on Advances in Destructive and Non-Destructive Analysis for Environmental Monitoring and Nuclear Forensics, Karlsruhe, Germany.
[22] A.M. Olsen, B. Richards, I. Schwerdt, S. Heffernan, R. Lusk, B. Smith, E. Jurrus, C. Ruggiero, L.W. McDonald, Quantifying morphological features of α-U3O8 with image analysis for nuclear forensics, Anal. Chem. 89 (5) (2017) 3177–3183.
[23] C. Ruggiero, J.J. Bloch, Morphological Analysis for Material Attribution (MAMA), Los Alamos National Laboratory, 2016.
[24] I. The Mathworks, MATLAB and Statistics Toolbox Release 2015b, Natick, Massachusetts, United States, 2015.
[25] S.I. Inc., JMP Pro Version 13.1.0, Cary, NC, United States, 2016.
[26] V.K. Pecharsky, P.Y. Zavalij, Fundamentals of powder diffraction and structural characterization of materials, Springer, 2009.
[27] X. Guo, D. Wu, H. Xu, P.C. Burns, A. Navrotsky, Thermodynamic studies of studtite thermal decomposition pathways via amorphous intermediates UO3, U2O7, and UO4, J. Nucl. Mater. 478 (2016) 158–163.
[28] T. Sato, Thermal decomposition of uranium peroxide hydrates, J. Appl. Chem. Biotechnol. 26 (4) (1976) 207–213.
[29] S.O. Odoh, J. Shamblin, C.A. Colla, S. Hickam, H.L. Lobeck, R.A. Lopez, T. Olds, J.E. Szymanowski, G.E. Sigmon, J. Neuefeind, W.H. Casey, M. Lang, L. Gagliardi, P.C. Burns, Structure and reactivity of X-ray amorphous uranyl peroxide, U2O7, Inorg. Chem. 55 (7) (2016) 3541–3546.
[30] R. Thomas, M. Rivenet, E. Berrier, I. de Waele, M. Arab, D. Amaraggi, B. Morel, F. Abraham, Thermal decomposition of (UO2)O2(H2O)2·2H2O: influence on structure, microstructure and hydrofluorination, J. Nucl. Mater. 483 (2017) 149–157.
[31] J. Plaue, Forensic Signatures of Chemical Process History in Uranium Oxides, Chemistry, University of Nevada, Las Vegas, 2013, p. 323.
[32] K.W. Kim, J.T. Hyun, K.Y. Lee, E.H. Lee, K.W. Lee, K.C. Song, J.K. Moon, Effects of the different conditions of uranyl and hydrogen peroxide solutions on the behavior of the uranium peroxide precipitation, J. Hazard Mater. 193 (2011) 52–58.
[33] E.H.P. Cordfunke, A.A. van der Giessen, Particle properties and sintering behaviour of uranium dioxide, J. Nucl. Mater. 24 (2) (1967) 141–149.
[34] X. Machuron-Mandard, C. Madic, Plutonium dioxide particle properties as a function of calcination temperature, J. Alloy. Compd. 235 (2) (1996) 216–224.
[35] S. Manna, P. Karthik, A. Mukherjee, J. Banerjee, S.B. Roy, J.B. Joshi, Study of calcinations of ammonium diuranate at different temperatures, J. Nucl. Mater. 426 (1–3) (2012) 229–232.

[36] D.S. Schwartz, L. Tandon, P.T. Martinez, Morphological Comparison of U3O8 Ore Concentrates from Canada Key Lake and Namibia Sources, Los Alamos National Laboratory, 2016, p. 25.
[37] C.E. Ruggiero, R.B. Porter, MAMA Software Features: quantified Attributes, Los Alamos National Laboratory, 2014.
[38] E.P. Hastings, C. Lewis, J. FitzPatrick, D. Rademacher, L. Tandon, Characterization of depleted uranium oxides fabricated using different processing methods, J. Radioanal. Nucl. Chem. 276 (2) (2008) 475–481.
[39] A.M. Olsen, B. Richards, I. Schwerdt, S. Heffernan, R. Lusk, B. Smith, E. Jurrus, C.E. Ruggiero, L.W. McDonald, Quantifying morphological features of α-U3O8 with image analysis for nuclear forensics, Anal. Chem. (2017).
[40] E. Vigneau, C. Loisel, M.F. Devaux, P. Cantoni, Number of particles for the determination of size distribution from microscopic images, Powder Technol. 107 (3) (2000) 243–250.
[41] I.T. Young, Proof without prejudice: use of the Kolmogorov-Smirnov test for the analysis of histograms from flow systems and other sources, J. Histochem. Cytochem. 25 (7) (1977) 935–941.